RSC Advances

ROYAL SOCIETY OF CHEMISTRY

www.rsc.org/advances

RSC Advances

ARTICLE

Tuning SEI formation on nanoporous carbon-titania composite sodium ion batteries anodes and performance with subtle processing changes

Received 00th January 20xx,
Accepted 00th January 20xx

DOI: 10.1039/x0xx00000x

www.rsc.org/

Jeongwoo Lee[a], Yu-Ming Chen[b], Yu Zhu[b], and Bryan D. Vogt[a,*]

The morphology of composite materials used in battery electrodes is critical to provide the requisite transport paths for ions and electrons to enable high performance. In this work, we describe a simple and scalable method to fine tune the morphology of carbon/TiO_2 composite through polymerization-induced phase separation of a mixture containing commercial TiO_2 nanoparticles, poly(hydroxyethyl methacrylate) (PHEMA), and photoacid generator (PAG) dissolved in furfuryl alcohol (FA, monomer). UV exposure converts the PAG to a strong acid that catalyzes the FA polymerization to quickly initiate the polymerization. The morphology is modulated by the molecular weight of PHEMA and FA concentration that impact the miscibility and mobility. The polymerized composite is carbonized to yield porous carbon/TiO_2 electrodes, but the cycling performance is dictated by the morphology that develops during phase separation. Electrochemical impedance spectroscopy (EIS) analysis illustrates that subtle changes in synthetic conditions can dramatically impact the electrical or ion conductance, primarily through modulation in the solid electrolyte interphase (SEI). A careful investigation of the SEI layer on the porous carbon/TiO_2 composites demonstrates a clear correlation between the SEI and the surface area of the porous anode as determined by transmission electron microscopy (TEM) and X-ray photoelectron spectroscopy (XPS). With selection of synthetic conditions to yield a modest surface area composite, sustainable anodes with stable capacity can be fabricated for use in Na ion batteries.

Introduction

Lithium-based batteries have dominated non-stationary energy storage devices on the basis of their high energy density and capacity associated with its lightweight, low redox potential, and ease of insertion.[1-4] However, one of the critical challenges for lithium-based batteries is cost,[5] which is partially driven by the high extraction costs of lithium metal and its limited natural abundance.[6, 7] Unlike lithium, sodium is one of the most naturally abundant elements (6th most common) with a crustal concentration estimated to be 3 orders of magnitude greater than lithium.[7] This abundance has recently led a resurgence in sodium-ion battery investigations, despite two major drawbacks compared to lithium. First, the increased size of sodium (1.06 Å) compared to lithium ion (0.76 Å) limits the intercalation rate of Na^+ and associated diffusion processes.[8] Second, the molar mass of sodium (23 g/mol) is 3 times more than that of lithium (6.9 g/mol), but both ions carry the same charge (+1); this produces a significant decrease in the specific capacity on a mass basis for sodium.[7] However in applications where cost dominates weight restrictions, such as grid energy storage, and in emergent markets, sodium ion batteries provide significant promise for energy storage.

Due to its low cost and abundance, hard carbon is a commonly used anode materials for sodium ion batteries.[9-11] A rate capacity between 100 and 300 mAh/g has been generally obtained for hard carbons, with the capacity dependent on both the allotrope and morphology,[7, 12-14] although Ponrouch *et al.*[11] have recently demonstrated a hard carbon anode with capacity surpassing 320 mAh/g. One intrinsic limitation associated with carbon is its limited charge storage on a volumetric basis (low mass density). Therefore, alternative materials for sodium ion battery anodes have been examined to obtain higher capacity. In particular, titanium dioxide (TiO_2) has been studied as an anode material in sodium ion batteries[8, 15-19] due to its low cost, long cycle life, and ecofriendliness.[8, 15-19] However, the electrical conductivity of TiO_2 is low. Therefore, composite anode materials for sodium ion batteries that combine the merits of carbon and TiO_2 have been extensively investigated.[20, 21] For example, Yang *et al.*[22] fabricated N-doped TiO_2 nanorods decorated with carbon dots with capacity of ~250 mAh/g, and carbon-coated TiO_2 nanoparticles by Jiang *et al.*[23] exhibited a capacity of ~240 mAh/g. Alternative composites based on nanosized binary elemental alloys such as SnSb/C (435 mAh/g)[24] and Sn–SnS–C (664 mAh/g)[25] can provide further improvements in the capacity, but at the expensive of cost and environmental impact.

A significant challenge with the development of high performance composite electrodes for sodium ion batteries is to understand how the morphology impacts the performance.[26] Ionic and electronic conduction pathways are critical to enable high

[a] Department of Polymer Engineering, University of Akron, Akron, OH 44325.
[b] Department of Polymer Science, University of Akron, Akron, OH 44325.
* To whom correspondence should be addressed: vogt@uakron.edu
Electronic Supplementary Information (ESI) available: Additional TEM micrographs, representative galvanostatic charge-discharge and cyclic voltammetry curves, pore size distributions, and XPS data. See DOI: 10.1039/x0xx00000x

performance, while high surface area electrodes imply a high contact area with the electrolyte, which should ease the ions flux across the electrode/electrolyte interface.[27, 28] However, the long term performance of high surface area electrodes is limited in many cases by the generation of the solid electrolyte interphase (SEI) layer. The SEI layer formation consumes electrolyte and alkali metal ions[29] and tends to result in an irreversible capacity loss during the initial charge cycle. However, the SEI layer is generally electronically insulating and ionically conducting to protect the electrolyte from further decomposition if the SEI is stable.[30] Agubra *et al.* have demonstrated that the electrolyte decomposition and subsequent SEI layer formation on an anode electrode increases the impedance in lithium ions.[31] Recently, analysis of the SEI formation on Na2Ti3O7 anodes revealed the reaction between a standard binder (polyvinylidene difluoride) and the electrolyte that leads to an unstable SEI layer.[32] However, the interplay between morphology and SEI layer formation in composite electrodes has not been thoroughly investigated for sodium ion batteries.

Here, we investigate the interplay between morphology, SEI formation and performance for carbon/TiO_2 composite anode electrodes for sodium ion batteries. The reversible capacity of these anodes for sodium ion batteries(< 130 mAh/g) is inferior to the state-of-the-art for carbon/TiO_2 (e.g. 155 mAh/g for microsphere C-TiO_2[33] and 242 mAh/g for carbon-coated TiO_2 nanoparticles[23]), but the fabrication of these composites is simple and tunable, based on polymerization-induced phase separation using inexpensive and commercially available materials. This method enables identification of key morphological aspects that impact the performance of the composites. In this case, commercial TiO_2 nanoparticles are dispersed in furfuryl alcohol solution containing poly(hydroxyethyl methacrylate), PHEMA, and a photoacid generator (PAG). UV exposure generates a superacid to induce polymerization to poly(furfuryl alcohol), PFA; PFA provides the carbon matrix of non-graphitizing char,[34] while PHEMA fully decomposes to yield pores during carbonization. The morphology of these porous carbon/TiO_2 composites can be readily controlled using the molecular weight of the PHEMA and relative concentration of components. This simple route to modulate the morphology enables improved understanding of the SEI formation in these composites for sodium ion batteries.

Experimental

Materials. Furfuryl alcohol (FA, 98%), ethyl alcohol (EtOH, ≥ 99.5%), *N*-methyl-2-pyrrolidone (NMP, 99.5%), and poly(vinylidene fluoride) (PVDF, M_n = 107 kDa) were obtained from Sigma-Aldrich and used as received without further purification. Poly(2-hydroxyethyl methacrylate) (PHEMA) with nominal M_w = 20 kg/mol (20K), 300 kg/mol (300K), and 1000 kg/mol (1000K) was purchased from Scientific Polymer Products, Inc. (Ontario, NY) and used as received. Titanium oxide (TiO_2, anatase, 15 nm) was purchased from Nanostructured & Amorphous Materials, Inc. The TiO_2 nanoparticles were separated from water by centrifugation (accuSpin™400, Fisher Scientific) at 7000 rpm for 5 min, and the highly concentrated TiO_2 slurry was re-dispersed into deionized water and EtOH using an ultrasonic cleaner (VWR® symphony™, operating frequency: 35 kHz, VWR International) to remove the surfactant dispersant and then collected again by centrifugation. This washing process was repeated 3 times. Rhodorsil PI2074 (CAS#: 178233-72-2) was obtained from Promerus, LLC (Brecksville, OH) and used as the photoacid generator. Sodium perchlorate ($NaClO_4$, 98%, Sigma Aldrich) dissolved in a 1:1 (v/v) mixture of ethylene carbonate (EC, 99%, Sigma Aldrich) and propylene carbonate (PC, 99.7%, Sigma Aldrich) was used as an electrolyte for battery testing. Na metal (99.8%, Acros Organics) was used as the counter electrode and copper foil (0.025 mm thick, Puratronic®) was used as a current collector of the anode electrode in the coin cells.

Fabrication of PHEMA/PFA/TiO_2 composites. In order to fabricate the composites, 0.35 g of PHEMA was dissolved in a mixture of FA (0.2, 0.3, 0.5, or 0.7 g) and 0.2 g EtOH. 0.3 g of TiO_2 was ultrasonically dispersed in 0.3 g EtOH and subsequently 1.5 mg of Rhodorsil PI2074 was dissolved in this suspension. This mixture was combined with the polymer solution and cast into a PTFE petri dish to a thickness of ~0.2 mm. FA polymerization was induced by broadband UV (Spectroline, 4500 μW/cm) exposure and polymerization was carried out at 60 °C for 10 min. The composite was pyrolyzed at 900 °C in N_2 at 1 °C/min to 650 °C with 3 h hold at 650 °C, 1 °C/min to 900 °C, and then hold at 900 °C for 1 h. The temperature was then decreased at 3 °C/min to room temperature.

Characterization. The morphology was characterized by transmission electron microscopy (TEM, JSM-1230, 120 kV, JEOL). Cross-sections of the composites, approximately 70 nm thick, were prepared by ultramicrotome (PT-PC PowerTome, RMC) using a diamond knife. To enable microtomed samples, the composite was embedded in epoxy resin (Embed-812 Resin, Electron Microscopy Sciences) that was hardened at 60 °C for 12 h. The specimens were supported on a 3.05 mm diameter Cu grid (01753-F, TED PELLA, Inc.). The mobility of precursor during FA photopolymerization is estimated by the suspension viscosity (Rotonetic™ 2 drive, Bohlin Gemini) through the initial stages of polymerization. During the measurement of viscosity, OmniCure® S2000 (200 W Mercury Arc, Lumen Dynamics) is used as the UV light source for *in-situ* FA photopolymerization. The pore texture was elucidated by Nitrogen adsorption-desorption isotherms (Micromeritics TriStar II instrument) at 77 K to determine the specific surface area by the Brunauer-Emmett-Teller (BET) method. The composition of the composite was estimated from thermogravimetric analysis TGA Q50 (TA Instrument) with a heating rate of 20 °C/min to 700 °C in air. To avoid excess water in the sample, the composite materials were dried overnight under vacuum at 85 °C. All mass loss was attributed to removal of carbon. Powder X-ray diffraction (Ultima IV, Rigaku, Japan) was used to confirm the crystal structure of TiO_2 particles. The diffractometer used Cu K_α radiation at 40 kV and 35 mA. The diffraction data was measured from 20° < 2θ < 60° with a step size of 0.04° and a rate of 1°/min. The XRD profiles were analysed for anatase and rutile content using the relative intensity ratio (RIR) method:

$$\frac{I_\alpha}{I_\beta} = K\frac{W_\alpha}{W_\beta}$$

where I_α and I_β are characteristic peak intensities of α and β phases, W_α and W_β are weight fractions of α and β respectively. K is a constant determined by calibration curve with known samples.[35] In

this case, the content was calculated using PDXL2 softwave (Rigaku Corporation, v2.1.3.4) with the RIR values for the anatase and rutile of 4.99 and 3.62. The chemical composition of the neat and charge-discharge cycled carbon/TiO_2 composite anodes was probed with X-ray photoelectron spectroscopy (XPS, PHI 5000 Versa probe II scanning XPS microprobe, ULVAC-PHI, Inc.) at a takeoff angle of 45 using pass energy of 11.75 eV at $2x10^{-6}$ Pa. High resolution scans at energies associated with C1s and O1s were performed to understand differences in the oxidation states. Each spectrum was collected using a monochromatic (Al K_α) x-ray beam (1486 eV) over a 200 μm diameter probing area. The peaks in the XPS spectra were fit using PHI MultiPak software.

Battery fabrication and testing. The carbonized composite materials were ground by mortar and pestle into a powder and mixed with carbon black (N330, Sid Richardson Co.), and PVDF (binder) at 85:5:10 (w/w/w) ratio for solids. A small amount of NMP (~30 - 40 mg to ~ 0.13 g of the carbonized composite powder) was added to generate concentrated slurry. The slurry was coated onto 13 mm (diameter) punched copper foil using a Mayer rod (RDS 22) and the coated foil was dried overnight in vacuum at 80 °C. Representative anodes contained approximately 1.5 mg of active material. CR2032 coin cells (MTI Corporation) were assembled in an Ar-filled glove box (O_2 < 0.5 ppm, H_2O < 0.5 ppm) using the composite on copper foil as the anode electrode, Na metal as the cathode electrode, Celgard® 3501 (Celgard, LLC.) as the separator, and 1 M solution of $NaClO_4$ in EC and PC (1:1 v/v) as the electrolyte.

The performance of the coin cells was determined using galvanostatic charge and discharge experiments with a battery tester (BST8-WA, MTI) at current densities between 10 and 50 mA/g. The potential window used was 0.01 - 2.00 V vs. Na/Na^+, consistent with prior studies for Na-ion batteries using TiO_2 as the active anode.[7, 16, 21] Cyclic voltammetry (CV) and electrochemical impedance spectroscopy (EIS) analysis were carried out in CR2032 coin cells using an electrochemical workstation CHI660D (CH Instruments). The CV was done in a potential range of 0.01-2.0 V at a scan rate of 0.1 mV/s, and the EIS was conducted with applied amplitude of 5 mV in the range of 100 kHz to 0.01 Hz, generally after cycling the electrodes for 30 or 40 charge-discharge cycles.

For the SEI layer characterization, the cycled coin cells were carefully opened using a disassembling machine (MSK-110D, MTI), and the carbon/TiO_2 composite electrodes were briefly rinsed by propylene carbonate and subsequently ethanol. The rinsed electrodes were dried in a vacuum oven at 80 °C before analyses. A reference as-produced electrode was prepared for comparison to the cycled electrodes. These reference electrodes were produced using the same concentrated slurry with carbon/TiO_2 composite, carbon black, PVDF, and NMP. Additionally, these control electrodes were assembled as coin cells with sodium metal, separator, and electrolyte, but no potential was applied to the control electrodes. The same disassembly and cleaning procedure was used for the control and cycled electrodes.

Results and discussion

Figure 1A illustrates the N_2 adsorption–desorption isotherms for the carbon/TiO_2 composites fabricated with varying molecular weight of PHEMA. These materials all exhibit type IV isotherms with a hysteresis loop at high relative pressures, P/P_0.[36] For the small molecular weight PHEMA, the hysteresis loop closes near $P/P_0 \sim 0.9$, which suggests the primary pores are connected by large mesopore windows. Conversely, the composite fabricated with the high molecular weight (1000K) PHEMA exhibits a much broader hysteresis loop that does not close until P/P_0~0.4. This suggests a broad distribution in window size between primary pores with small mesopores connecting the larger pores. The surface area of these composites increases with the molecular weight of PHEMA from 43.03 (20K) to 63.83 m^2/g (1000K), which corresponds with changes in morphology of the carbon/TiO_2 composites (Figure S1). The pores of the carbon/TiO_2 composite are significantly larger for the composite produced using 20K PHEMA (Figure S1A) than the carbon/TiO_2 composites from 300K (Figure S1B) and 1000K PHEMA (Figure S1C). The morphology of porous carbon/TiO_2 composites pyrolyzed from PHEMA/FA/TiO_2 appears to be controlled by the mobility of the precursor suspension that decreases as the molecular weight of PHEMA increases. To confirm the lower mobility in the high molecular weight precursor suspensions, the viscosity of the solution during FA polymerization is used as a surrogate for mobility (Figure S2). Although the viscosity of all solutions increases during polymerization, a much larger viscosity and increase in viscosity as polymerization proceeds are found for the higher molecular weight of PHEMA. Additionally, the TiO_2 nanoparticles appear to be more aggregated in the composites formed with higher molecular weight of PHEMA. For the composites fabricated with higher molecular weight PHEMA, the distribution of TiO_2 nanoparticles appears to become increasingly more heterogeneous with the nanoparticles preferentially segregated near the pore interface.

Figure 1B illustrates the galvanostatic charge-discharge curves for pure TiO_2 (includes carbon black) and the carbon/TiO_2 composite (fabricated with 20K PHEMA). First, the capacity of the TiO_2 electrode is only approximately 20 mAh/g on the first discharge and this fades to less than 10 mAh/g after only 3 cycles. This poor cycling performance of the TiO_2 anode is attributed to structural pulverization during the insertion/desertion of sodium.[37] The composite exhibits a much larger initial capacity of approximately 120 mAh/g and the fade is almost negligible in comparison to the pure TiO_2 electrode. Additional galvanostatic charge discharge curves for the other composites are shown in Figures S3 and S4. To better illustrate the cycling stability of the composite electrodes, Figure 1C shows the impact of molecular weight of PHEMA used in the fabrication of the anode on the capacity of the porous carbon/TiO_2 composite anodes for a range of charge−discharge rates. Although high surface area generally improves the capacity by increasing the flux across the electrode/electrolyte interface,[27] the capacity of these porous carbon/TiO_2 composite anodes decreases with increasing surface area. This behavior is somewhat surprising as the capacitive fade on cycling is quite small as shown in Figure 1B. The capacity is stable for all materials examined after approximately 10 cycles. Increasing the current density from 10 mA/g (about 0.1 C) up to 50 mA/g (about 0.8 C) decreases the capacity for all samples; however, the highest capacity is always found for the composite fabricated with the lowest molecular weight PHEMA. However, the capacity of

these electrodes is less than one might expect from anatase TiO_2.[8, 15-19] The high temperature associated with carbonization of the PFA could also lead to conversion of the anatase[42] to rutile[43] phase. As determined from XRD (Figure S5), the rutile fraction in the TiO_2 increases from 1.7 % to 10.4 % after carbonization of PFA/PHEMA/TiO_2 composite The capacity of rutile has been demonstrated to be inferior to anatase for sodium ion batteries,[8] so the capacity performance is not unexpected.

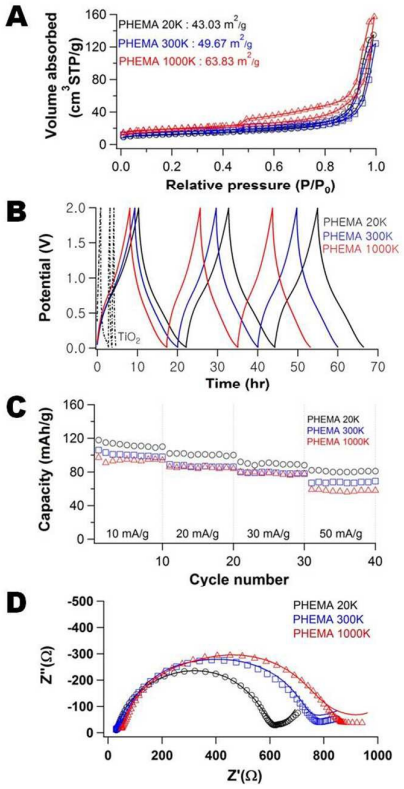

Figure 1. (A) N_2 adsorption and desorption isotherms, (B) Galvanostatic charge-discharge cycling for the composite electrodes at 10 mA/g, (C) impact of rate on capacity during galvanostatic cycling, and (D) Nyquist plots of the porous carbon/TiO_2 composite fabricated using 0.35 g PHEMA/0.3 g FA/0.3 g TiO_2 as a function of molecular weight of PHEMA: 20K (o), 300K (□), and 1000K (Δ).

Figure 1C shows the EIS spectra of the carbon/TiO_2 composite electrodes after 40 charge-discharge cycles as a function of the molecular weight of PHEMA used in their fabrication. These spectra provide insight into the surface (ion adsorption and desorption) and bulk (ion diffusion) processes associated with charge storage.[38] Nyquist plots for these electrodes exhibit a semi-circle at high frequency and then a linear increase at low frequency associated with the Na^+ ion diffusion in the anode material (Warburg impedance).[39] As the molecular weight of PHEMA increases, the diameter of semi-circle increases (increased the charge transfer resistance[9]). Additionally, the ohmic resistance, *R*, associated with the bulk carbon, grain boundary and interface resistances determined at high frequency (Z' ~ tens of Ω) increases slightly as the molecular weight of the PHEMA used in the fabrication increases. This behavior is somewhat unexpected as the composition for the electrodes are identical. This increased $R_{\square}$ suggests that the extent of the SEI formation is dependent on the pore morphology. The higher surface area electrodes exhibit increased resistance from both *R* and the SEI layer. At low frequency after the semi-circle, the impedance is associated with the semi-infinite diffusion of the Na^+ ions. However, the impedance for the composite fabricated with the highest molecular weight PHEMA behaves unexpectedly with Z'' nearly independent of Z'. This decrease of Warburg slope (semi-infinite diffusion) as a function of the molecular weight of PHEMA is attributed directly to the diffusion limitations of the system.[40] To better quantify the differences in the structure of the composite electrodes, the EIS data were fit to an electric circuit model (Figure S6). The bulk resistance (includes electrolyte, separator and electrode) increases from 3.9 W to 15.0 W to 24.5 W as the molecular weight of PHEMA used in the fabrication increases. Additionally, the resistance attributed to the formation of the SEI layer is increased almost by an order of magnitude for the electrode fabricated with 1000K PHEMA in comparison to using the 20K PHEMA. The SEI layer appears to evolve through the first 10 charge-discharge cycles (Figure S7) The formation of the SEI layer is further investigated through cyclic voltammetry as shown in Figure S8. Redox peaks were observed between 0.01 and 1.0 V. These peaks are attributed to the insertion and extraction of sodium ion at the carbon/TiO_2 composite.[41] In the first cathodic scan, there are current peaks at potentials greater than 1.0 V, whereas these peaks fade in the second and subsequent scans. This evolution is attributed to the irreversible formation of the SEI layer.[41] The charge/discharge cycle appears to be stabilized after 10 cycles.

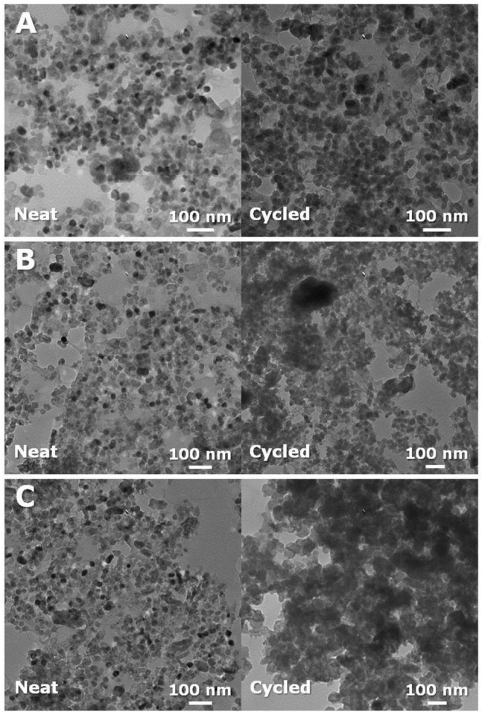

Figure 2. TEM images of carbon/TiO_2 composite anodes as-produced (left) and after 40 charge-discharge cycles (right) fabricated with (A) 20K, (B) 300K, and (C) 1000K PHEMA using 0.35 g PHEMA/0.3 g FA/0.3 g TiO2 for the precursor.

To better understand the origins of the differences in impedance, Figure 2 illustrates the morphology of the neat composite anodes (left) and after 40 charge-discharge cycles (right) as a function of molecular weight of PHEMA used in the fabrication. Consistent with the N_2 sorption isotherms, the neat composite anodes contain smaller pores as the molecular weight of PHEMA used in their fabrication increases (Figure S9). We attribute this pore size dependence to the mobility during the FA polymerization (Figure S2). These differences impact how the morphology changes from the SEI layer as shown in Figure 2. Smaller pore sizes lead to greater changes in the morphology. This behavior is consistent with SEI formation in lithium ion electrodes where the decomposition is proportional to the surface area of the carbon electrode.[44] The increase in dark spots in the TEM micrographs is attributed to the oxygen-rich SEI products (Na_2CO_3, R-OCO_2Na, and R-CH_2ONa).[45, 46] As shown on right panels in Figure 2, the density of these dark spots increases with increasing surface area. The increased SEI on electrodes fabricated with high molecular weight PHEMA likely leads to the high impedance of the electrodes (Figure 1C).

XPS spectra provide complementary information about the SEI layer after 40 charge-discharge cycles (as shown in Figure S10). We select 40 cycles as the SEI layer is stabilized by this cycle. Table 1 illustrates the composition changes of C, O and Na between as-produced and cycled electrodes due to the formation of SEI layer on the surface of electrodes. As a result, the molar ratio of O and Na to C increases; for instance, the molar ratio of C : O : Na for the composite anode fabricated with 20K PHEMA changes from 1 : 0.3 : 0 to 1 : 1.6 : 1.1 because of the decomposition of the electrolyte (a solution of $NaClO_4$ in EC and PC) and the formation of the passivating SEI layer from the breakdown of the electrolyte on the surface of the electrodes.

Table 1. Surface elemental composition from XPS of carbon/TiO_2 composite anodes fabricated with 20K, 300K, and 1000K PHEMA using 0.35 g PHEMA/0.3 g FA/0.3 g TiO_2 for the precursor for the as-produced composite and after 40 charge-discharge cycles

PHEMA	As-produced						Cycled					
	C%	O%	Na%	Ti%	Cl%	F%	C%	O%	Na%	Ti%	Cl%	F%
20K	64.3 ±1.7	20.1 ±7.2	0	4.6 ±2.1	0	16.7 ±0.5	27.1 ±1.1	42.7 ±0.9	29.3 ±1.0	0.1 ±0.04	0.7 ±0.04	0.2 ±0.1
300K	70.8 ±4.8	16.3 ±4.8	0	2.1 ±0.2	0	10.2 ±8.9	28.2 ±0.8	43.9 ±1.6	26.5 ±0.5	0.1 ±0.03	0.9 ±0.1	0.4 ±0.1
1000K	82.7 ±1.3	13.6 ±0.2	0	1.2 ±1.2	0	2.3 ±1.4	36.7 ±4.1	40.5 ±1.0	22.0 ±2.0	0.1 ±0.04	0.5 ±0.4	0.3 ±0.2

To better understand the composition of the SEI layers, high-resolution XPS is used to investigate the 1s binding of C as shown in Figure 3. The strong C1s peak at ~284.6 eV is assigned to C-C bonds in the electrode and the C-C bonds are expected to be present in the carbon component of the neat composite. The oxygen-rich components associated with the SEI layer formed by electrolyte (EC and PC) decomposition are associated with the C-O-C bonds at ~286.2 eV and O-C=O bonds at ~289 eV.[47, 48] Intriguingly, as a function of the molecular weight of PHEMA used (20K vs. 1000K) in their fabrication, the peak intensity and peak area of O-C=O decrease from 521 C/s (44 % of C area) to 330 C/s (26.2 % of C area), whereas the peak intensity and peak area of C-O-C increase from 212 C/s (17.8 % of C area) up to 274 C/s (24.0 % of C area). The increases of C-O-C peak intensity and area are attributed to the electrolyte (EC and PC) decomposition, where the C=O bonds in EC and PC are reduced to C-O.[49] The enhanced C-O-C bonds when the electrode is fabricated with higher M_n PHEMA is expected based on the increased SEI formation in theTEM micrographs.

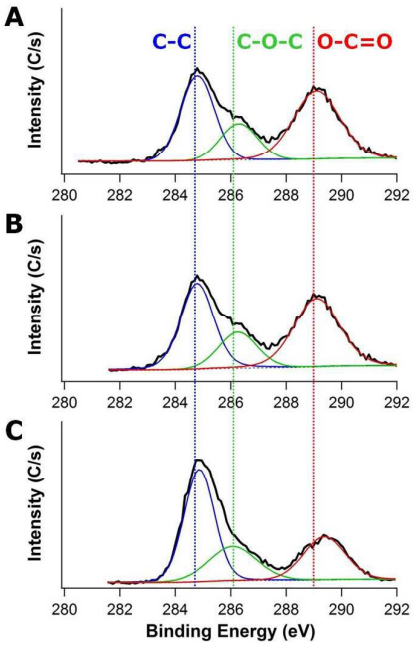

Figure 3. XPS spectra of carbon/TiO_2 composite anodes after 40 charge-discharge cycles fabricated with (A) 20K, (B) 300K, and (C) 1000K PHEMA using 0.35 g PHEMA/0.3 g FA/0.3g TiO_2 for the precursor.

The largest pore size leads to the best performance for the composites examined. The mobility of the PHEMA appears to determine the morphology of the composites (high mobility = larger pores) and thus 20K PHEMA is used for examining composition effects on performance. The carbon:TiO_2 ratio can be easily modulated by the FA concentration in the precursor suspension. Figure 4A illustrates how the N_2 adsorption–desorption isotherms for the carbon/TiO_2 composites are impacted by the concentration of FA used in their fabrication. At low concentration of FA (0.2 g), the surface area is at a maximum (74.1 m^2/g), but then the surface area increases with increasing amount of FA in the precursor from a minimum of 43.0 (0.3 g) to 63.3 m^2/g (0.7 g). The increase in surface area can be rationalized from the changes in morphology of the carbon/TiO_2 composites (Figure S11), where the pore size generally decreases as the FA concentration increases. The maximum in surface area at the lowest FA loading is attributed to exposed TiO_2 nanoparticles in the composite (Figure S11A). These exposed nanoparticles provide roughness that increases the surface area.

The pores of the carbon/TiO_2 composite are significantly larger for the composite produced using 0.3 g FA (Figure S11B) than the

carbon/TiO_2 composites from 0.5 g FA (Figure S11C) and 0.7 g FA (Figure S11D). The Barrett-Joyner-Halenda (BJH) average pore sizes of the different composites using 0.3 g, 0.5 g, and 0.7 g of FA are ~24 nm, ~16 nm, and ~14 nm, respectively. For this series of samples, the TiO_2 nanoparticles are mostly covered by the carbon produced from the FA and thus the surface area scales inversely with pore size as expected (as the volume adsorbed is similar between the samples from Figure 4A). Thus, the morphology of porous carbon/TiO_2 composites pyrolyzed from PHEMA/FA/TiO_2 can also be controlled by the amount of FA used in the synthesis, in addition to the PHEMA molecular weight.

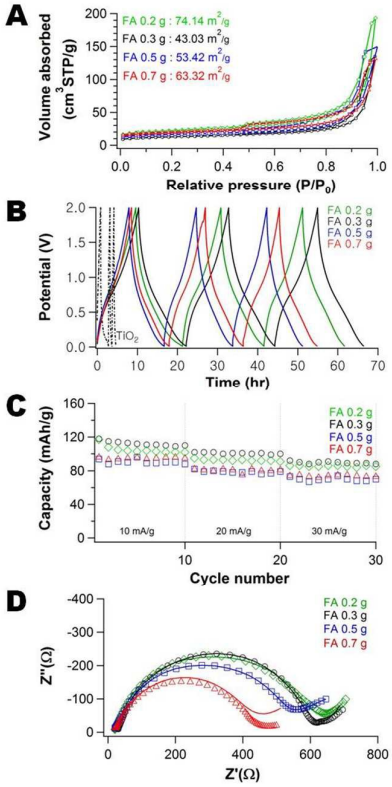

Figure 4. (A) N_2 adsorption and desorption isotherms, (B) Galvanostatic charge and discharge curves for the first 3 cycles, (C) Galvanostatic cycling, and (D) Nyquist plots of the porous carbon/TiO_2 composite fabricated using 0.35 g PHEMA (20K)/FA/0.3 g TiO_2 as a function of amount of FA: 0.2 (◊), 0.3 (○), 0.5 (□), and 0.7 g (Δ).

Figure 4B illustrates the galvanostatic charge-discharge curves of the porous carbon/TiO_2 composites as well as the neat TiO_2 anode (containing carbon black). A significantly higher and more stable capacity is obtained from the composites in caparison to the neat TiO_2 anode. Figure 4C illustrates how the composition and morphology of the active carbon/TiO_2 impacts the capacity stability. As the current density increases from 10 mA/g (about 0.1 C) up to 30 mA/g (about 0.4 C), there is a decrease in the capacity by approximately 25 %, irrespective of the composition of the composite. Increasing the FA content generally leads to a decrease in performance. The difference in carbon content is relatively small with the carbon content increasing from 12 to 18 wt% for the composites using 0.2 and 0.7 g FA (see Figure S12). There is also a concurrent increase in surface area (consistent with molecular weight effect where surface area is inversely related to performance). The lowest FA content composite (0.2 g FA) exhibits a slightly lower capacity than the composite fabricated with 0.3 g FA; this material has the lowest carbon content (12 wt %) and the highest surface area, so the performance is anomalous for this series of materials. Two probable reasons are the limited carbon content leads to poor electrical conductivity and/or the difference in surface chemistry where more TiO_2 nanoparticles are exposed, which could lead to a SEI layer that limits Na^+ transport.

To better understand these differences in performance, the EIS spectra of the carbon/TiO_2 composite electrodes are examined (Figure 4D). As the carbon content increases, the impedance decreases at high frequency and the slope of the linear regions decreases at low frequencies. The Na^+ ion diffusion into the electrode is hindered at the higher carbon content. To understand this behavior, the morphology and chemical changes of the cycled composite anodes are investigated by TEM and XPS.

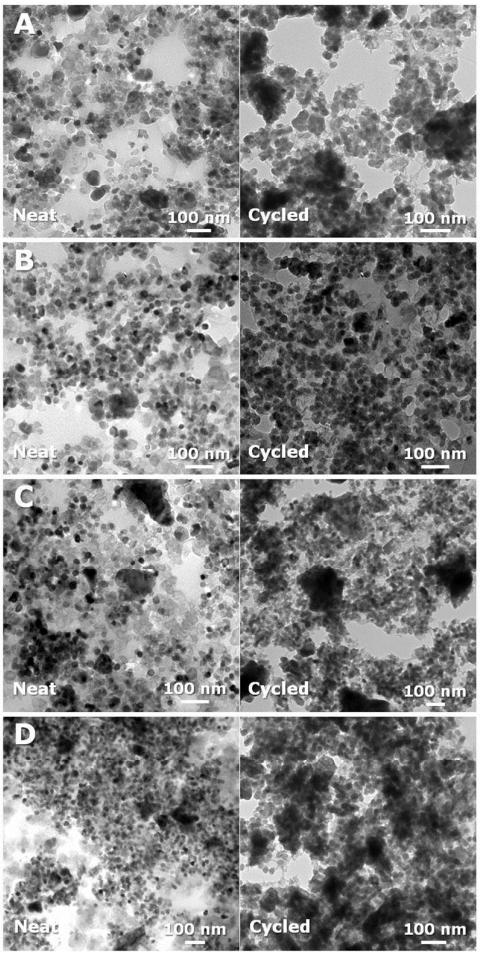

Figure 5. TEM images of carbon/TiO_2 composite anodes as-produced (left) and after 30 charge-discharge cycles (right) fabricated with 0.35g PHEMA (20K) / 0.3g TiO_2/FA of (A) 0.2 g (12 wt% carbon), (B) 0.3 g (15 wt% carbon), (C) 0.5 g (16 wt% carbon), and (D) 0.7 g (18 wt% carbon).

The change of morphology between neat and cycled composites is shown in Figure 5. The neat composite anodes (left side in Figure 5) contain smaller pores as the amount of FA used in their fabrication increases (Figure S13). The FA content controls the amount of carbon in the composites after pyrolysis of PHBMA/PFA/TiO_2. From the TEM micrographs (right side in Figure 5), it is possible to distinguish the low electron density carbon (light), the oxygen-rich SEI layers (darker regions) and the TiO_2 nanoparticles (almost black). Thus generally, the SEI layer content increases as the carbon content of the composite materials increases. However, the lowest carbon content composite anode (Figure 5A) appears to exhibit an increased SEI layer (dark spots) like composite anodes with higher carbon loading. We hypothesize that the exposed TiO_2 nanoparticles lead to this increased SEI content.

Table 2. Surface elemental composition from XPS of anodes as-produced and after 30 charge-discharge cycles fabricated with different carbon contents of carbon/TiO_2 composites

Carbon content	As-produced						Cycled					
	C%	O%	Na%	Ti%	Cl%	F%	C%	O%	Na%	Ti%	Cl%	F%
12 wt%	75.8 ±0.9	17.8 ±0.6	0	6.4 ±0.3	0	0.2 ±0.3	40.6 ±10.2	35.6 ±3.9	20.8 ±6.2	0.1 ±0.02	2.7 ±0.6	0.2 ±0.08
15 wt%	64.3 ±1.7	20.1 ±7.2	0	4.6 ±2.1	0	16.7 ±0.5	27.1 ±1.1	42.7 ±0.9	29.3 ±1.0	0.1 ±0.04	0.7 ±0.04	0.2 ±0.1
16 wt%	71.5 ±7.8	20.6 ±7.5	0	4.1 ±3.1	0	6.8 ±2.7	23.5 ±2.7	41.4 ±1.1	30.7 ±1.9	0.2 ±0.05	0.5 ±0.4	0.6 ±0.05
18 wt%	75.2 ±12.2	15.9 ±11.2	0	4.8 ±2.5	0	4.2 ±3.1	37.7 ±6.5	39.8 ±2.7	21.2 ±3.6	0.1 ±0.01	1.2 ±0.05	0.3 ±0.1

To further investigate the SEI layer formation, XPS spectra are obtained for the as-produced electrodes and after 30 charge-discharge cycles (Figure S14). Table 2 illustrates how the composition changes during cycling due to the formation of SEI layer. At low carbon content (12 wt%), the molar ratio of O and Na to C after 30 charge-discharge cycles increases much less than the other three anodes. We attribute this difference to the presence of exposed TiO_2 nanoparticles in the low carbon content sample that leads to a different SEI layer, which is consistent with our hypotheses regarding the performance and impedance data for this sample.

High-resolution XPS spectra for the 1s binding of C and O are shown in Figure 6. The area ratio of C-C bond to carbon-oxygen bonds (C-O-C and O-C=O) decreases from 1 : 1.51 to 1 : 0.78 as the FA content increases, which corresponds to an increase in the carbon content of the anode from 15 wt% to 18 wt% (as shown in Table 3). This is unusual as the SEI layer appears to be more prevalent for the higher carbon content anodes from the TEM micrographs (Figure 5), but there are less carbon-oxygen bonds near the surface relative to C-C bonds for the high carbon content anodes. This is counter to expectations based on the survey scan (Table 2). To better understand this behavior, high-resolution XPS spectra for O1s are investigated to identify C=O (~531 eV), C-O (~532.5 eV), and C-OH (~533 eV).[50] As the carbon content increases (except for the low carbon, 12 wt %, outlier), the peak area of C=O decrease from 64.6 % to 52.1 %, whereas the peak areas of C-O and C-OH increase from 10.9 % to 27.1 %, all on the basis of the total area for the oxygen peaks. These data are consistent reduction of the electrolyte (EC and PC) as the C=O bonds are reduced to C-O.[49]

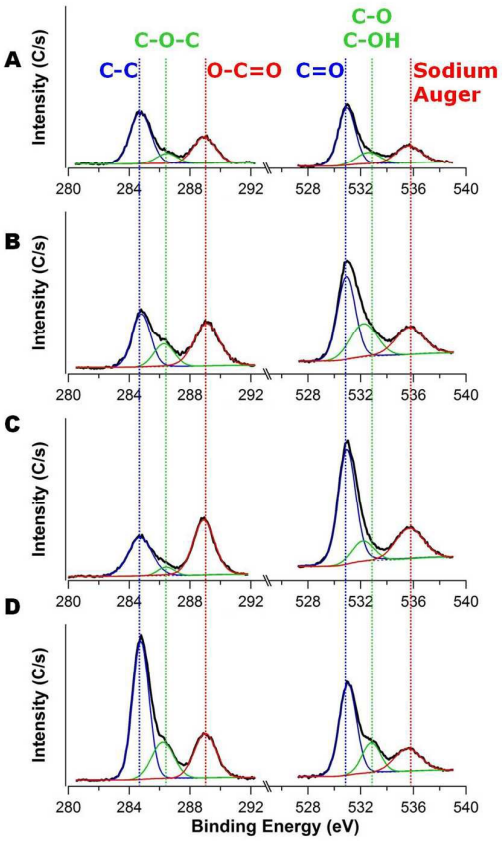

Figure 6. XPS spectra examining C1s (left) and O1s (right) for the anodes after 30 charge-discharge cycles fabricated with different carbon contents of carbon/TiO_2 composite: (A) 12 wt%, (B) 15 wt%, (C) 16 wt%, and (D) 18 wt%.

Table 3. The changes of peak areas from high resolution XPS spectra as a function of carbon contents in the composite anodes after 30 charge-discharge cycles

C1s / Carbon content	C-C (~284.6 eV)	C-O-C (~286.2 eV)	O-C=O (~289 eV)	C-C : (C-O-C + O-C=O)
12 wt%	57.8 ± 0.6 %	11.1 ± 0.5 %	31.1 ± 0.1 %	1 : 0.73
15 wt%	39.9 ± 2.2 %	21.4 ± 3.6 %	38.7 ± 1.5 %	1 : 1.51
16 wt%	40.6 ± 0.5 %	6.3 ± 0.02 %	53.1 ± 0.5 %	1 : 1.46
18 wt%	56.3 ± 0.01 %	19.5 ± 0.1 %	24.2 ± 0.01 %	1 : 0.78
O1s / Carbon content	**C=O (~531 eV)**	**C-O, C-OH (~532.8 eV)**	**Na Auger (~535.5 eV)**	**(C=O + C-O, C-OH) : Na Auger**
12 wt%	58.8 ± 1.2 %	14.8 ± 1.6 %	26.5 ± 0.3 %	1 : 0.36
15 wt%	64.6 ± 0.4 %	10.9 ± 1.0 %	24.8 ± 0.6 %	1 : 0.33
16 wt%	63.9 ± 1.3 %	11.0 ± 2.1 %	24.6 ± 1.3 %	1 : 0.33
18 wt%	52.1 ± 2.7 %	27.1 ± 3.2 %	20.9 ± 0.5 %	1 : 0.26

These XPS data focused on O1s provide an additional advantage to understand the SEI layer formation as the Na auger is visible in the energy window examined. The nature of the SEI layer formed on carbons depends on the location: the basal plane, which consists of sp^2 carbon atoms (C-C bonds), typically generates SEI that is rich in organic compounds, whereas the edge sites, which contain dandling bonds and various capping moieties (e.g., hydrogen, hydroxyl, carbonyl and carboxyl groups), typically generates SEI that is rich in inorganic compounds.[51, 52] Table 3 illustrates the change of the ratio between oxygen-rich substances (C=O, C-O, and C-OH peaks) and sodium (Na Auger peak) as a function of the carbon content after 30 charge-discharge cycles. This ratio is the largest for the lowest carbon content (1:0.37) and decreases to a minimum at the highest carbon content (1:0.26). We attribute this difference to the propensity of organic-rich SEI to form on the basal plane of carbon, so the higher carbon content (18 wt%) should lead to additional SEI.

These results illustrate the interplay between surface area, composition, surface chemistry and pore size on determining the performance of anatase TiO_2-carbon composite anodes for sodium ion batteries. In particular, these factors impact the SEI layer formation. Higher surface areas of the composite materials lead to additional SEI, while increasing the carbon content of the composite also generates more SEI. The SEI layer can adversely impact the long-term performance of the anodes with a decrease in capacity and an increase in impedance.

Conclusions

The morphology of porous carbon/TiO_2 composites was tuned using the composition and molecular weight of the porogen in the precursor via a simple polymerization induced phase separation process using a renewable carbon source (furfuryl alcohol). The SEI layer formation increases on the anode having larger surface area, but the nature of the SEI appears to depend on minor perturbations in the composition of the anode. The composite with high carbon content has more sp^2 carbon atoms (C-C bonds) and tends to produce a thick SEI layer that consists of primarily organic compounds (oxygen-rich substances). This high SEI layer formation limits sodium ion diffusion and impacts performance with an increase in the impedance and decreases in capacity as the carbon content in the composites increases. This simple polymerization induced phase separation method provides a facile route to teasing out how seemingly minor changes in composition and morphology impact the performance. This method could provide a route to help to better design electrode materials for sodium ion batteries by understanding interplay between structure and performance.

Acknowledgements

This work has been partial supported by the National Science Foundation under grant CBET-1336057. Acknowledgment is made to the Donors of the American Chemical Society Petroleum Research Fund partial support of this research through award 53739-ND7. The authors acknowledge the assistance of Zhorro Nikolov with XPS and Bojie Wang with TEM measurements.

References

1. J. M. Tarascon and M. Armand, *Nature*, 2001, **414**, 359-367.
2. J. B. Goodenough and Y. Kim, *Chem. Mater.*, 2010, **22**, 587-603.
3. A. L. M. Reddy, S. R. Gowda, M. M. Shaijumon and P. M. Ajayan, *Adv. Mater.*, 2012, **24**, 5045-5064.
4. M. G. Kim and J. Cho, *Adv. Funct. Mater.*, 2009, **19**, 1497-1514.
5. A. Shcherbakova, A. Kleit and J. Cho, *Appl. Energ.*, 2014, **125**, 93-102.
6. C. Bommier, W. Luo, W. Y. Gao, A. Greaney, S. Q. Ma and X. Ji, *Carbon*, 2014, **76**, 165-174.
7. J. Lee, Y. M. Chen, Y. Zhu and B. D. Vogt, *ACS Appl. Mater. Inter.*, 2014, **6**, 21011-21018.
8. D. Su, S. Dou, and G. Wang, *Chem. Mater.*, 2015, **27**, 6022-6029.
9. T. Chen, Y. Liu, L. Pan, T. Lu, Y. Yao, Z. Sun, D. H. C. Chua and Q. Chen, *J. Mater. Chem. A*, 2014, **2**, 4117-4121.
10. W. Luo, J. Schardt, C. Bommier, B. Wang, J. Razink, J. Simonsen and X. L. Ji, *Journal of Materials Chemistry A*, 2013, **1**, 10662-10666.
11. A. Ponrouch, A. R. Goni and M. R. Palacin, *Electrochem. Commun.*, 2013, **27**, 85-88.
12. K. Tang, L. Fu, R. J. White, L. Yu, M.-M. Titirici, M. Antonietti and J. Maier, *Adv. Energy Mater.*, 2012, **2**, 873-877.
13. S. Wenzel, T. Hara, J. Janek and P. Adelhelm, *Energ. Environ. Sci.*, 2011, **4**, 3342-3345.
14. R. Alcantara, P. Lavela, G. F. Ortiz and J. L. Tirado, *Electrochem. Solid St.*, 2005, **8**, A222-A225.
15. Z. H. Bi, M. P. Paranthaman, P. A. Menchhofer, R. R. Dehoff, C. A. Bridges, M. F. Chi, B. K. Guo, X. G. Sun and S. Dai, *J. Power Sources*, 2013, **222**, 461-466.
16. L. M. Wu, D. Buchholz, D. Bresser, L. G. Chagas and S. Passerini, *J. Power Sources*, 2014, **251**, 379-385.
17. Z. Yan, L. Liu, J. Tan, Q. Zhou, Z. Huang, D. Xia, H. Shu, X. Yang and X. Wang, *J. Power Sources*, 2014, **269**, 37-45.
18. L. Wu, D. Bresser, D. Buchholz, G. A. Giffin, C. R. Castro, A. Ochel and S. Passerini, *Adv. Energy Mater.*, 2015, **5**.
19. H. Xiong, M. D. Slater, M. Balasubramanian, C. S. Johnson and T. Rajh, *J. Phys. Chem. Lett.*, 2011, **2**, 2560-2565.
20. D. Bresser, B. Oschmann, M. N. Tahir, F. Mueller, I. Lieberwirth, W. Tremel, R. Zentel and S. Passerini, *J. Electrochem. Soc.*, 2015, **162**, A3013-A3020.
21. H. A. Cha, H. M. Jeong and J. K. Kang, *J. Mater. Chem. A*, 2014, **2**, 5182-5186.
22. Y. Yang, X. Ji, M. Jing, H. Hou, Y. Zhu, L. Fang, X. Yang, Q. Chen and C. E. Banks, *J. Mater. Chem. A*, 2015, **3**, 5648-5655.
23. Y. Ge, H. Jiang, J. Zhu, Y. Lu, C. Chen, Y. Hu, Y. Qiu and X. Zhang, *Electrochim. Acta*, 2015, **157**, 142-148.
24. L. Xiao, Y. Cao, J. Xiao, W. Wang, L. Kovarik, Z. Nie and J. Liu, *Chem. Commun.*, 2012, **48**, 3321-3323.
25. L. Wu, X. Hu, J. Qian, F. Pei, F. Wu, R. Mao, X. Ai, H. Yang and Y. Cao, *J. Mater. Chem. A*, 2013, **1**, 7181-7184.
26. C. Jo, Y. Park, J. Jeong, K. T. Lee and J. Lee, *Acs Appl. Mater. Inter.*, 2015, **7**, 11748-11754.
27. S. Goriparti, E. Miele, F. De Angelis, E. Di Fabrizio, R. P. Zaccaria and C. Capiglia, *J. Power Sources*, 2014, **257**, 421-443.
28. Y. Ishii, Y. Kanamori, T. Kawashita, I. Mukhopadhyay and S. Kawasaki, *J. Phys. Chem. Solids*, 2010, **71**, 511-514.

29. P. Arora, R. E. White and M. Doyle, *J. Electrochem. Soc.*, 1998, **145**, 3647-3667.
30. E. Markevich, V. Baranchugov, G. Salitra, D. Aurbach and M. A. Schmidt, *J. Electrochem. Soc.*, 2008, **155**, A132-A137.
31. V. Agubra and J. Fergus, *Materials*, 2013, **6**, 1310-1325.
32. M. A. Munoz-Marquez, M. Zarrabeitia, E. Castillo-Martinez, A. Eguia-Barrio, T. Rojo and M. Casas-Cabanas, *Acs Appl. Mater. Inter.*, 2015, **7**, 7801-7808.
33. S.-M. Oh, J.-Y. Hwang, C. S. Yoon, J. Lu, K. Amine, I. Belharouak and Y.-K. Sun, *Acs Appl. Mater. Inter.*, 2014, **6**, 11295-11301.
34. J. F. Mareche, D. Begin, G. Furdin, S. Puricelli, J. Pajak, A. Albiniak, M. Jasienko-Halat and T. Siemieniewska, *Carbon*, 2001, **39**, 771-773.
35. H. Chen, S. Chen, L. Li and S. Jin, *Propell. Explos. Pyrot.*, 2008, **33**, 467-471.
36. K. Sing, *Colloid. Surfaces. A*, 2001, **187**, 3-9.
37. K.-T. Kim, G. Ali, K. Y. Chung, C. S. Yoon, H. Yashiro, Y.-K. Sun, J. Lu, K. Amine and S.-T. Myung, *Nano Lett.*, 2014, **14**, 416-422.
38. S. B. Yoon, J. P. Jegal, K. C. Roh and K. B. Kim, *Journal of the Electrochemical Society*, 2014, **161**, H207-H213.
39. S. Tanaka, A. Doi, T. Matsui and Y. Miyake, *J. Power Sources*, 2013, **228**, 24-31.
40. R. P. Ramasamy, C. Feger, T. Strange and B. N. Popov, *J. Appl. Electrochem.*, 2006, **36**, 487-497.
41. D. Yan, C. Yu, Y. Bai, W. Zhang, T. Chen, B. Hu, Z. Sun and L. Pan, *Chem. Commun.*, 2015, **51**, 8261-8264.
42. T. Chen, G. H. Guai, C. Gong, W. Hu, J. Zhu, H. Yang, Q. Yan and C. M. Li, *Energy Environ. Sci.*, 2012, **5**, 6294-6298.
43. W. Hu, L. Li, W. Tong, G. Li and T. Yan, *J. Mater. Chem.*, 2010, **20**, 8659-8667.
44. R. Fong, U. Vonsacken and J. R. Dahn, *J. Electrochem. Soc.*, 1990, **137**, 2009-2013.
45. L. Ji, M. Gu, Y. Shao, X. Li, M. H. Engelhard, B. W. Arey, W. Wang, Z. Nie, J. Xiao, C. Wang, J.-G. Zhang and J. Liu, *Adv. Mater.*, 2014, **26**, 2901-2908.
46. S. Komaba, W. Murata, T. Ishikawa, N. Yabuuchi, T. Ozeki, T. Nakayama, A. Ogata, K. Gotoh and K. Fujiwara, *Adv. Funct. Mater.*, 2011, **21**, 3859-3867.
47. J. T. Lee, N. Nitta, J. Benson, A. Magasinski, T. F. Fuller and G. Yushin, *Carbon*, 2013, **52**, 388-397.
48. V. Eshkenazi, E. Peled, L. Burstein and D. Golodnitsky, *Solid State Ionics*, 2004, **170**, 83-91.
49. Y. An, P. Zuo, C. Du, Y. Ma, X. Cheng, J. Lin and G. Yin, *Rsc Adv.*, 2012, **2**, 4097-4102.
50. P. Verma, P. Maire and P. Novak, *Electrochim. Acta*, 2010, **55**, 6332-6341.
51. W. Yuan, Y. Zhou, Y. Li, C. Li, H. Peng, J. Zhang, Z. Liu, L. Dai and G. Shi, *Sci. Rep.*, 2013, **3**.
52. K. Zaghib, G. Nadeau and K. Kinoshita, *J. Power Sources*, 2001, **97-8**, 97-103.

Graphical abstract

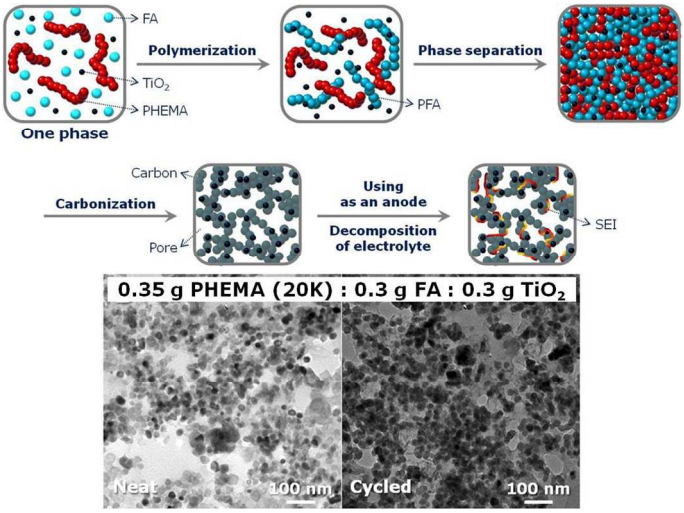

SEI formation on porous TiO_2-carbon composites is sensitive to the structure, which can be tuned by the composition of the precursor slurry or the molecular weight of the porogen polymer.